



Adaptive weighted curvature-based active contour for ultrasonic and 3T/5T MR image segmentation



Zhi-Feng Pang^a, Mengxiao Geng^{a,b}, Lan Zhang^c, Yanru Zhou^c, Tieyong Zeng^d, Liyun Zheng^e, Na Zhang^b, Dong Liang^b, Hairong Zheng^b, Yongming Dai^f, Zhenxing Huang^{b,*}, Zhanli Hu^{b,*}

^a School of Mathematics and Statistics, Henan University, Kaifeng, China

^b The Lauterbur Research Center for Biomedical Imaging, Shenzhen Institute of Advanced Technology, Chinese Academy of Sciences, Shenzhen, China

^c First Affiliated Hospital of Henan University of Chinese Medicine, Zhengzhou, China

^d Department of Mathematics, The Chinese University of Hong Kong, Shatin, Hong Kong

^e Shenzhen United Imaging Research Institute of Innovative Medical Equipment, Shenzhen, China

^f MR Collaboration, Central Research Institute, United Imaging Healthcare, Shanghai, China

ARTICLE INFO

Article history:

Received 25 September 2022

Revised 14 November 2022

Accepted 2 December 2022

Available online 7 December 2022

Keywords:

Medical image segmentation

Adaptive weight

High-order total variation

Heat kernel convolution

ABSTRACT

Image segmentation is a complex and core technique for disease diagnosis or image-guided surgery in the medical image domain. However, low-quality images, such as images with weak edges and intensity inhomogeneities, may bring considerable challenges for radiologists. In this paper, we propose an adaptive weighted curvature-based active contour model by coupling heat kernel convolution and adaptively weighted high-order total variation for medical image segmentation to improve diagnosis effectiveness. To reduce the computational complexity, the heat kernel convolution operation is applied to approximate the perimeter of a segmentation curve. In addition, the weighted parameter included in the high-order total variation term can be automatically evaluated based on an adaptive input image to emphasize local structures and increase segmentation accuracy. Since the proposed method is a smoothing optimization model, the alternating direction method of multipliers is introduced to translate the original problems into several easily solvable subproblems. The numerical experimental results on ultrasonic and 3T/5T MRI datasets demonstrate that the proposed model is quite efficient and robust compared with several traditional segmentation methods.

© 2022 Elsevier B.V. All rights reserved.

1. Introduction

Medical images include images obtained by computed tomography (CT) [1], positron emission tomography (PET) [2], magnetic resonance imaging (MRI) [3], ultrasound [4] and other medical imaging equipment. In the actual application field of computer-aided diagnosis (CAD) and image-guided surgery systems, the segmentation of organs or tumors from a medical scan helps clinicians make an accurate diagnosis, plan the surgical procedure, and propose treatment strategies [5,6]. However, medical image processing is complex and diverse, and the formation of images is easily affected by noise and intensity inhomogeneity [7]. In addition, there are great differences among patients, and the shape of the human tissue structure is also complex. Hence, one of the principal problems is how to develop some automatic, accurate, and robust medical image segmentation methods.

In the past few decades, many researchers have made great progress in developing many segmentation. However, there is still no universally perfect image segmentation method. In particular, scholars have reached a consensus on the general law of image segmentation, and a considerable number of related research methods and results have been produced. For different application scenarios, different segmentation models, such as data-driven models [8–11] and model-driven models [12,13], have been proposed. Data-based models need a massive amount of data for training, which causes a high computational burden [14]. In addition, there is still no universal approach that works well for a segmentation target in a complex environment whose background cannot be trivially subtracted, especially the small lesions cannot get effective annotation data [15,16]. To this end, this paper mainly considers model-driven models.

Among many model-driven models, active contour models [17–19] are traditional models with good properties that can obtain segmentation results with smooth and closed contours and manage the changes in the topology structure by using the level set

* Corresponding authors.

E-mail addresses: zx.huang1@siat.ac.cn (Z. Huang), zl.hu@siat.ac.cn (Z. Hu).

function (LSF) to describe the curve evolution. According to the difference in the curve evolution, active contour models are roughly grouped into three major categories: edge-based models [20,21], region-based models [22,23] and hybrid-based models [24,25]. The Chan-Vese (CV) model [26] is one of the most representative models among region-based models, and it mainly approximates segmentation regions with a piecewise constant function. However, solving the CV model based on the level set method (LSM) may cause the model to become stuck in a local minimum due to its nonconvexity, and it is sensitive to the initialization. To overcome this drawback, Chan et al. [27] reformulated the CV model into a convex minimization problem by relaxing the binary constraint into a convex set. It is proven that the global optimal labeled solution can be obtained by thresholding any value of the solution in [0,1]. Since the traditional active contour models cannot reach the optimal accuracy standard, Bresson et al. in [28] proposed a global minimizer for the active contour model (GMAC) by coupling an edge-based model into a region-based model and then used an operator splitting method to solve it. To obtain better segmentation performance for an intensity inhomogeneous image, many improved CV-based models have been proposed by coupling local image information. In [18,29], Li et al. proposed a local binary fitting (LBF) model by using a convolutional kernel function to extract the local image information. Their aim was to utilize local image information with a spatially varying weight to control the scalable parameter and extract local features. In [23], Zhang et al. proposed a local intensity fitting (LIF) model to segment intensity inhomogeneous images. Li et al. [30] proposed a region-based method by using a local intensity clustering (LIC) property of the image intensity and defined a local clustering criterion function in a neighborhood of each point. This local clustering criterion function was then integrated with respect to the neighborhood center for a global given criterion. Based on the curve evolution technique, Krnidis and Chatzis [31] presented a fuzzy energy for active contours (FEAC) method to detect an object in an image. This fuzzy energy uses motivation power to evolve an active contour and then stops the motivation process when the desired object boundary is found. Based on the FEAC, Fang et al. [32] proposed a region-edge-based active contour driven by hybrid and local fuzzy region-based energy (HLFRA), which is mainly used to calculate the difference between the old and new energy functions to update the pseudo LSF during the curve evolution.

From a numerical computation perspective, the effectiveness of a segmentation model also depends on the robustness of the numerical algorithm used. Among the model-driven models, some models need to employ the total variation term to describe the length of the segmentation curves. However, due to the nonsmoothing of the total variation term, we usually need to introduce some operator splitting methods, such as the alternating direction method of multipliers (ADMM) and the primal dual method [33,34], to solve the proposed model. Furthermore, we can also analyse and deal with this problem on influence of disturbances, modeling errors, various uncertainties in the real systems [35–37]. To maintain the numerical stability of the algorithm used, some parameters included in the algorithm and model need to be manually set and adjusted until the segmentation results are optimal. This increases the computational complexity. Recently, Wang et al. [38] proposed using an iterative convolution-thresholding method (ICTM) to approximately replace the total variation in terms of the heat kernel convolution operation [39,40]. Hence, an iterative convolution-thresholding method can be designed to approximately solve the CV model. In addition, to improve the segmentation accuracy, Y. Yang et al. in [41] proposed a weight-based segmentation method, the weights of which were automatically estimated based on the edge information of the observed images. However, we notice that the weights used in the total variation

are not suitable since the weight is more robust in high-order total variation problems. Motivated by the above observations, this paper proposes a novel adaptive weighted curvature-based active contour for the image segmentation problem and then proposes an efficient numerical algorithm to solve it. The main contributions can be summarized as follows.

- (1) The heat kernel convolution characteristic function in the proposed model is implemented to approximate the perimeter of the segmentation curve, which can effectively reduce the computational complexity. Specifically, we introduce the heat kernel convolution characteristic function to reduce the number of parameters that must be manually adjusted in the WBHV model, which greatly enhances the effectiveness of the proposed model.
- (2) The weight included in the high-order total variation term can be automatically adjusted according to the input image to describe the features of the local structure and improve the segmentation accuracy. Additionally, due to the nonsmoothing of the high-order total variation term, we employ the ADMM by alternatively dividing the original problem into several simple subproblems and optimizing them.
- (3) The proposed model is extended from two-phase segmentation to multi-phase segmentation in the experiments, which reflects that our proposed model can be arbitrarily extended to higher dimensions for medical images. In particular, we perform two-phase segmentation on ultrasonic and 3T/5T MRI datasets and extend it to four-phase segmentation on brain MR images.

The rest of the paper is organized as follows. We briefly review some methods in Section II. In Section III, we propose a novel adaptive weighted curvature-based active contour. Then we introduce the numerical algorithm based on the ADMM and give the corresponding solution method in this section. Some numerical comparisons are arranged to illustrate the efficiency of the proposed method in Section IV. Finally, we report our discussion and conclusion in Section V.

2. Related works

This section mainly reviews some models related to our proposed model. Let $\Omega \subset \mathbb{R}^2$ be a bounded open connected set, Γ be a compact curve in Ω , and $I(x) : \Omega \rightarrow \mathbb{R}$ be a given image¹. Without loss of generality, we restrict $I(x) \in [0, 1]$ and hence $I(x) \in L^\infty(\Omega)$. c_1 and c_2 are positive, and they are the average values of the pixels inside and outside the boundary Γ for the segmentation region.

2.1. The CV model

In [42], Mumford and Shah proposed an energy minimization problem which approximates the true solution by finding optimal piecewise smooth approximations. However, it is very challenge for solving the MS model due to the nonconvexity and the singularity. As a simplification of the Mumford-Shah model, Chan and Vese (CV) in [26] considered to solve the following optimization problem

$$\min_{c_1, c_2, \Gamma} \frac{\lambda}{2} \int_{\Omega_1} (I(x) - c_1)^2 dx + \frac{\lambda}{2} \int_{\Omega_2} (I(x) - c_2)^2 dx + L(\Gamma), \quad (1)$$

where λ is a positive parameter and $L(\Gamma)$ is the total length of all the smooth arcs in the set Γ . Ω_1 and Ω_2 represent the internal and external regions of the segmentation target, respectively. As a

¹ This paper assumes that the image $I(x)$ is the gray image. Without any confusions, we use the vectors $x := (x_1, x_2)$ and $y := (y_1, y_2)$ to denote the variables in the image domain Ω . Additionally, for the convenience of writing, this paper omits the variable x in $I(x)$ as I .

global ACM, the CV model is analogous to the global characteristics of an image region. Consequently, its segmentation accuracy decreases for images with intensity inhomogeneity.

2.2. The GMAC model

In order to couple with the advantages of the edge-based models and the region-based models, Bresson et al. [28] proposed a fast global minimization of the active contour (GMAC) model. This model avoids the disadvantage of the level set method for preserving the distance function where the active contour needs to be periodically reinitialized. In general, after obtaining the values of c_1 and c_2 , the GMAC model can be written as

$$\min_{u(x) \in [0,1]} \lambda \int_{\Omega} ((I(x) - c_1)^2 - (I(x) - c_2)^2) u dx + \int_{\Omega} g(I(x)) |\nabla u| dx, \quad (2)$$

where $g(I(x)) = \frac{1}{1+\gamma|\nabla I(x)|^2}$ denotes an edge detection function and $|\nabla u| = \sqrt{u_{x_1}^2 + u_{x_2}^2}$. Here the positive parameter γ controls the weight of edge detection function $g(I(x))$.

2.3. The LBF model

The CV model (1) and the GMAC model (2) are unsuitable to segment the inhomogeneous image. To this end, Li et al. [18,29] proposed a Local Binary Fitting (LBF) model via utilizing the local prior image information as follows:

$$\begin{aligned} \min_{\phi, c_1, c_2} & \int_{\Omega} \lambda_1 \int_{\Omega_1} k(x-y) |I(x) - f_1(y)|^2 H(\phi(x)) dx dy \\ & + \int_{\Omega} \lambda_2 \int_{\Omega_2} k(x-y) |I(x) - f_2(y)|^2 (1 - H(\phi(x))) dx dy \\ & + \nu \int_{\Omega} |\nabla H(\phi(x))| dx + \frac{\mu}{2} \int_{\Omega} (|\nabla \phi(x)| - 1)^2 dx, \end{aligned} \quad (3)$$

where λ_1 , λ_2 , ν and μ are the positive parameters, $f_1(y)$ and $f_2(y)$ are two fitting functions that are closest to the local intensity values in Ω_1 and Ω_2 when the contour is on the object boundary. $k(x-y)$ is a Gaussian kernel function. $H(\cdot)$ is a Heaviside function. And $\phi(x)$ is a level set function, whose zero level contour partitions the image domain Ω into two disjoint regions $\Omega_1 = \{x : \phi(x) > 0\}$ and $\Omega_2 = \{x : \phi(x) < 0\}$. The third term as the distance regularization term is used to maintain the stability of the level set evolution, and the forth term as the length regularization term is used to measure the length of zero level set to avoid small and isolated regions in the segmentation result.

2.4. The LIC model

Although the LBF model (3) has better performance accuracy and computational efficiency, its numerical method is highly sensitive to the initial contour position and then maybe stuck in then local minima due to the nonconvexity. To assume that pixel intensities in the small local set are approximately equal to one another and can be viewed as a cluster with center, Li et al. [30] proposed a local intensity clustering model (LIC)

$$\begin{aligned} \min_{\phi, B, c_1, c_2} & \int_{\Omega} \lambda_1 \int_{\Omega_1} k(x-y) |I(x) - B(y)c_1|^2 H(\phi(x)) dx dy \\ & + \int_{\Omega} \lambda_2 \int_{\Omega_2} k(x-y) |I(x) - B(y)c_2|^2 (1 - H(\phi(x))) dx dy \\ & + \nu \int_{\Omega} |\nabla H(\phi(x))| dx + \frac{\mu}{2} \int_{\Omega} (|\nabla \phi(x)| - 1)^2 dx \end{aligned} \quad (4)$$

for the intensity inhomogenous segmentation, where the bias field $B(y)$ is smooth and slow. The LIC model (4) adds some information

of the bias field and the intensity information, so it has the ability of the image segmentation and simultaneous correction of the bias field. However, it still is sensitive to the initialization and can fall into the local minima due to the nonconvexity.

2.5. The ICTM model

For the energy functional-based model, we can use the total variation to describe the length of the segmentation region based on the binary indicator function and the coarea formula. However, the nonsmoothing of the total variation increases the numerical difficulty. So the authors in [38] proposed an iterative convolution-thresholding method (ICTM) to approximate the total variation in the CV model. This method is not only simple and easy to implement but also suitable for different segmentation cases. More specifically, the proposed ICTM method is considered to solve the following problem:

$$\begin{aligned} \min_{c_1, c_2, u \in [0,1]} & \lambda \int_{\Omega} (I - c_1)^2 u + (I - c_2)^2 (1 - u) dx \\ & + \sqrt{\frac{\pi}{\tau}} \int_{\Omega} u G_{\tau} * (1 - u) dx, \end{aligned} \quad (5)$$

where $G_{\tau}(x) = \frac{1}{4\pi\tau} \exp\left(-\frac{|x|^2}{4\tau}\right)$ with standard derivation τ , $*$ represents the convolution operator and λ is a fixed parameter.

2.6. The HLFRA model

To segment the image with the high noise and the intensity inhomogeneity and force the initial contour to move towards the exact boundary of the segmentation object, Fang et al. [32] proposed a region-edge-based active contours driven by hybrid and local fuzzy region-based energy (HLFRA) by combining the region energy and the edge energy as

$$\min_u E_{HFR}(u) + E_{LFR}(u) + E_E(u), \quad (6)$$

where $E_{HFR}(u)$ represents the hybrid fuzzy region term, $E_{LFR}(u)$ represents the local fuzzy region term and $E_E(u)$ represents the edge energy. Here these terms are respectively defined by

$$\begin{aligned} E_{HFR}(u) &= \lambda_1 \int_{\Omega} [u(x)]^m p(x) (I(x) - (q_b + c_1)/2)^2 dx \\ &+ \lambda_2 \int_{\Omega} [1 - u(x)]^m p(x) (I(x) - (q_s + c_2)/2)^2 dx, \\ E_{LFR}(u) &= \rho_1 \int_{\Omega} [u(x)]^m \int_{\Omega} \omega(x, y) p(x) (I(y) - q_b)^2 dy dx \\ &+ \rho_2 \int_{\Omega} [1 - u(x)]^m \int_{\Omega} \omega(x, y) p(x) (I(y) - q_s)^2 dy dx, \\ E_E(u) &= \varphi_1 \int_{\Omega} \delta(u - 0.5) |\nabla(u - 0.5)| dx \\ &+ \frac{\varphi_2}{2} \int_{\Omega} (1 - |\nabla(u - 0.5)|)^2 dx, \end{aligned}$$

where λ_1 , λ_2 , ρ_1 , ρ_2 , φ_1 , and φ_2 are six positive parameters, $p(x) = \frac{1}{1+|\nabla k_{\sigma} * I(x)|^2}$ is an edge detector. $q_s = \text{mean}(I(y)|y \in \Omega_x \cap u(y) < 0.5)$ and $q_b = \text{mean}(I(y)|y \in \Omega_x \cap u(y) > 0.5)$ are two average intensities and $u(y)$ is the fuzzy membership function in the local image region Ω_x , $\omega(x, y) = \frac{1}{1+|x-y|}$ is a spatial weight that can extract the local image information, m is a weight exponent, and $\delta(u) = \frac{1}{\pi} \frac{\epsilon}{\epsilon^2 + u^2}$ is a Dirac function for a positive constant ϵ . The model (6) works very efficient for segmenting the degraded image, but how to balance so many parameters is very difficult in order to get more robust segmentation results.

2.7. The WBHV model

For low-quality images, it is essential to describe the edge and the segmentation region efficiently. In [41], Y. Yang et al. proposed a weighted bounded Hessian variational model (WBHV), in which the weights were automatically estimated based on the edge information of the observed images. In particular, by minimizing the combined first- and second-order regularizer, the model could overcome a shortage of the total variation. The WBHV model can be written as

$$\begin{aligned} & \min_{u \in [0,1]} \int_{\Omega} \alpha(I) |\nabla u| dx + \int_{\Omega} \beta(I) |\nabla^2 u| dx \\ & + \lambda \int_{\Omega} ((I - c_1)^2 - (I - c_2)^2) u dx, \end{aligned} \quad (7)$$

where $|\nabla^2 u| = \sqrt{u_{x_1 x_1}^2 + u_{x_1 x_2}^2 + u_{x_2 x_1}^2 + u_{x_2 x_2}^2}$, $\alpha(I)$ and $\beta(I)$ are used to capture the edge information as follows:

$$\alpha(I) = \left| \nabla \left(\frac{1}{\sqrt{1 + |\nabla I|^2}} \right) \right| \text{ and } \beta(I) = \frac{1}{\sqrt{1 + |\nabla I|^2}}. \quad (8)$$

Model (7) is a nonsmooth optimization problem, and its segmentation speed and accuracy depend on the numerical algorithm used. Although we can use the splitting method to solve it, adjusting many parameters seriously affects the effectiveness of the model (7).

3. The proposed method

In this section, we propose an improved model based on the ICTM model in (5) and the WBHV model in (7) for the multiphase segmentation problem. For this model, the heat kernel convolution operation is applied to approximate the perimeter of the segmentation curve, which can reduce the computational complexity. Moreover, the weight in the high-order total variation term can be automatically evaluated based on the input image to emphasize the local structure and improve the segmentation accuracy. Since the proposed model includes a nonsmooth term that couples the Hessian operator into the L^1 -norm, the alternating direction method of multipliers (ADMM) can be employed to solve it. Here, we assume that the image domain Ω is partitioned into n subdomains Ω_j such that $\Omega = \cup_{j=1}^n \Omega_j$ and $\Omega_i \cap \Omega_j = \emptyset$ if $i \neq j$. For every segmentation region, we introduce an indicator function

$$u_i(x) = \begin{cases} 1, & \text{if } x \in \Omega_i \\ 0, & \text{otherwise} \end{cases}$$

for $i = 1, \dots, n$ and a constrained set² as

$$\mathcal{C} = \left\{ \mathbf{u} \mid u_i = [0, 1] \text{ and } \sum_{i=1}^n u_i = 1 \right\}$$

for $\mathbf{u} = (u_1, u_2, \dots, u_n)$.

Although two weights $\alpha(I)$ and $\beta(I)$ included in the (7) model can describe the local information and then give a robust segmentation result, we notice that the weight $\alpha(I)$ has little influence on the segmentation result for medical images, as shown by the numerical implementations in Section IV. In addition to the segmentation problem, the accuracy and effectiveness mainly depend on how the local information is described and the numerical method used. With the help of the above motivations, we propose the fol-

lowing segmentation method:

$$\left\{ \begin{array}{l} c_i := \mathcal{D}(u_i) = \frac{\int_{\Omega} l u_i dx}{\int_{\Omega} u_i dx} \\ \mathbf{u} = \operatorname{argmin}_{\mathbf{u} \in \mathcal{C}} \mathcal{M}(u, c) := \sqrt{\frac{\pi}{\tau}} \sum_{i=1}^n \sum_{j=1, j \neq i}^n \int_{\Omega} u_i G_{\tau} * u_j dx \end{array} \right. \quad (9a)$$

$$\left. \begin{array}{l} + \int_{\Omega} \beta(I) |\nabla^2 \mathbf{u}| dx + \lambda \sum_{i=1}^n \int_{\Omega} (c_i - I)^2 u_i dx \end{array} \right. \quad (9b)$$

for $i = 1, \dots, n$, where c_i is positive since $u_i \in [0, 1]$ and I is the inputting image, $\beta(I)$ is defined in (8) and G_{τ} is the heat kernel with a scale parameter τ .

In the proposed segmentation schemes in (9a) and (9b), the main challenge is how to efficiently solve the optimization problem in (9b). More specifically, the main challenge is addressing non-convex and the nonsmooth problems. For nonsmooth problems, we need to decouple the Hessian operator ∇^2 from the Frobenius norm. Hence, we employ ADMM [43]. Actually, the basic idea of ADMM is to introduce some auxiliary variables to breakdown a complicated convex problem into several simple subproblems, where each one is efficiently solvable via a suitable formula. To derive ADMM, we introduce the variable $\mathbf{z} = (z_1, z_2, \dots, z_n)$ and then rewrite problem (9b) as a constrained optimization problem

$$\left\{ \begin{array}{l} \min_{\mathbf{u}, \mathbf{z}} \sqrt{\frac{\pi}{\tau}} \sum_{i=1}^n \sum_{j=1, j \neq i}^n \int_{\Omega} u_i G_{\tau} * u_j dx + \int_{\Omega} \beta(I) |\mathbf{z}| dx \\ + \lambda \sum_{i=1}^n \int_{\Omega} (c_i - I)^2 u_i dx + \delta_{\mathcal{C}}(\mathbf{u}), \text{ s.t. } \mathbf{z} = \nabla^2 \mathbf{u}, \end{array} \right. \quad (10)$$

where $\delta_{\mathcal{C}}(\mathbf{u})$ is the characteristic function $\delta_{\mathcal{C}}(\mathbf{u}) = 0$ if $\mathbf{u} \in \mathcal{C}$ and $\delta_{\mathcal{C}}(\mathbf{u}) = +\infty$ if $\mathbf{u} \notin \mathcal{C}$.

Based on the well-known augmented Lagrangian method and introducing the Lagrangian multiplier $\boldsymbol{\eta} = (\eta_1, \eta_2, \dots, \eta_n)$, we can reformulate (10) into the following saddle point problem:

$$\min_{\mathbf{u}, \mathbf{z}} \max_{\boldsymbol{\eta}} \mathcal{L}_{\mathbf{C}}(\mathbf{u}, \mathbf{z}; \boldsymbol{\eta}). \quad (11)$$

Here, the augmented Lagrangian function $\mathcal{L}_{\mathbf{C}}(\mathbf{u}, \mathbf{z}; \boldsymbol{\eta})$ is defined by

$$\begin{aligned} \mathcal{L}_{\mathbf{C}}(\mathbf{u}, \mathbf{z}; \boldsymbol{\eta}) = & \sqrt{\frac{\pi}{\tau}} \sum_{i=1}^n \sum_{j=1, j \neq i}^n \int_{\Omega} u_i G_{\tau} * u_j dx + \lambda \sum_{i=1}^n \int_{\Omega} (c_i - I)^2 u_i dx \\ & + \delta_{\mathbf{C}}(\mathbf{u}) + \int_{\Omega} \beta(I) |\mathbf{z}| dx + \int_{\Omega} (\mathbf{z} - \nabla^2 \mathbf{u}) \boldsymbol{\eta} dx \\ & + \frac{\gamma}{2} \int_{\Omega} |\mathbf{z} - \nabla^2 \mathbf{u}|^2 dx, \end{aligned}$$

where γ is a penalty parameter. Under the ADMM framework, we can use the following iterative scheme:

$$\left\{ \begin{array}{l} \mathbf{u}^{k+1} = \operatorname{argmin}_{\mathbf{u}} \mathcal{L}_{\mathbf{C}}(\mathbf{u}, \mathbf{z}^k; \boldsymbol{\eta}^k) \\ \mathbf{z}^{k+1} = \operatorname{argmin}_{\mathbf{z}} \mathcal{L}_{\mathbf{C}}(\mathbf{u}^{k+1}, \mathbf{z}; \boldsymbol{\eta}^k) \end{array} \right. \quad (12a)$$

$$\left. \begin{array}{l} \boldsymbol{\eta}^{k+1} = \boldsymbol{\eta}^k + \gamma (\mathbf{z}^{k+1} - \nabla^2 \mathbf{u}^{k+1}) \end{array} \right. \quad (12b)$$

$$\left. \begin{array}{l} \boldsymbol{\eta}^{k+1} = \boldsymbol{\eta}^k + \gamma (\mathbf{z}^{k+1} - \nabla^2 \mathbf{u}^{k+1}) \end{array} \right. \quad (12c)$$

to solve the problem in (11). In the following, we consider solving every subproblem in detail.

- (1) Subproblem (12a) is the smooth optimization problem. To improve the effectiveness of the numerical computation, we linearize its objective function at \mathbf{u}^k , and then we can obtain the following approximated form:

$$u_i^{k+1} = \operatorname{argmin}_{\mathbf{u}} \sum_{i=1}^n \int_{\Omega} u_i \Psi_i^k dx + \delta_{\mathbf{C}}(\mathbf{u}), \quad (13)$$

where

$$\Psi_i^k = 2 \sqrt{\frac{\pi}{\tau}} \sum_{j=1, j \neq i}^n G_{\tau} * u_j^k + \lambda (c_i - I)^2 + \gamma \operatorname{div}^2 \left(\nabla^2 u_i^k - z_i^k - \frac{\eta_i^k}{r} \right). \quad (14)$$

² For the sake of convenience, this section omits the variable x in $u_i(x)$ as u_i .

Here, div^2 denotes the adjoint operator of the Hessian operator ∇^2 . Obviously, the minimum can be attained at

$$u_i^{k+1} = \begin{cases} 1, & \text{if } i = \arg\min_{\ell=1,\dots,n} \Psi_\ell^k, \\ 0, & \text{otherwise.} \end{cases} \quad (15)$$

(2) The subminimization problem in (12b) is a typical $\ell^1 - \ell^2$ minimization problem with a spatially varying parameter, and we can rewrite it as

$$\min_{\mathbf{z}} \int_{\Omega} \beta(I) |\mathbf{z}| dx + \frac{\gamma}{2} \int_{\Omega} \left| \mathbf{z} - \left(\nabla^2 \mathbf{u}^{k+1} - \frac{\boldsymbol{\eta}^k}{\gamma} \right) \right|^2 dx.$$

Based on the shrinkage-soft operator, the closed-form solution can be obtained by

$$\mathbf{z}^{k+1} = \max \left\{ \left| \mathbf{T}^k \right| - \frac{\beta(I)}{\gamma}, 0 \right\} \frac{\mathbf{T}^k}{\left| \mathbf{T}^k \right|}, \quad (16)$$

where $\mathbf{T}^k = \nabla^2 \mathbf{u}^{k+1} - \boldsymbol{\eta}^k / \gamma$.

In summary, the efficient ADMM is proposed to deal with the scheme described by (9a)-(9b), which is detailed in [Algorithm 1](#).

Algorithm 1: The ADMM to solve the proposed scheme in (9a)-(9b).

Input: The image I and parameters λ , τ and γ .
1 Initialization: $\mathbf{u}^0, \mathbf{z}^0 = 0, \boldsymbol{\eta}^0 = \mathbf{0}; \bar{k} = 0$.
2 while (Stopping conditions are not satisfied) **do**
 3 Compute $\mathbf{c}^{\bar{k}}$ by $c_i^{\bar{k}} = \mathcal{D}(\mathbf{u}_i^{\bar{k}+1})$ in (9a).
 4 **while** ($l = 1, \dots, L$) **do**
 5 | Compute $(\mathbf{u}^{k+1}, \mathbf{z}^{k+1}, \boldsymbol{\eta}^{k+1})$ by (12a)-(12c).
 6 **end**
 7 Set $\mathbf{u}_i^{\bar{k}+1} := \mathbf{u}_i^{k+1}$ for $i = 1, 2, \dots, n$ and then go to Step 3.
 8 **end**

Output: Segmentation result $\mathbf{u} := \mathbf{u}^{\bar{k}+1}$.

4. Experiments and results

In this section, we use the proposed scheme (9a)-(9b) to segment some ultrasound images and 3T/5T MR images to show its reasonability and robustness compared with several state-of-the-art model-based methods, such as the CV [26], GMAC [28], ICTM [38], WBHV [41], HLFRA [32], LBF [29] and LIC [30] methods.

All the numerical experiments are conducted in MATLAB (R2020a) on a Windows 10 (64 bit) desktop computer with an Intel Core i9 3.70 GHz processor and 128 GB of RAM. The comparison models are programmed according to the related references. To compare the segmentation quality, we choose several indices, such as the Jaccard similarity (JS) [44], segmentation accuracy (SA) [45], F1-Score [41] and Kappa coefficient (κ) [41], to quantify the segmentation effectiveness. These indicators are specifically expressed as

$$\begin{aligned} JS &= \frac{|S_1 \cap S_2|}{|S_1 \cup S_2|}; SA = \frac{TP + TN}{TP + TN + FP + FN}; F1 - \text{Score} \\ &= \frac{2 \times TP}{2 \times TP + FN + FP}; \kappa = \frac{SA - M}{1 - M}. \end{aligned}$$

Here, S_1 and S_2 are the segmentation result in this experiment and the ground truth, respectively. Parameter M is defined by

$$M = \frac{(TP + FN)H + (FP + TN)Q}{(H + Q)^2},$$

where $H = TP + FP$, and $Q = FN + TN$. TP (true positive), TN (true negative), FP (false positive), and FN (false negative) correspond to the segmented actual regions, correctly unsegmented regions, detected false regions, and undetected actual regions, respectively. Obviously, the JS, SA, F1-Score, and κ values range from 0 to 1. 1 indicates that the result of the model is exactly identical to the ground truth, and 0 indicates that the result of the model is completely opposite from the ground truth. JS, SA and F1-Score indicators are most commonly used for image segmentation. In particular, Kappa coefficient is utilized to evaluate the consistency between the segmentation results of the model and the ground truths and frequently cooperating with SA.

4.1. Parameter rule

In the experiment, to stop [Algorithm 1](#), we arrive at the maximum iteration when $K_{\max} = 100$ or the related error (RE) is

$$RE = \frac{\|\mathbf{u}^{k+1} - \mathbf{u}^k\|_1}{\|\mathbf{u}^{k+1}\|_1} \leq 10^{-3}.$$

For the motioned models, the parameters are mainly divided into algorithm-based parameters and model-based parameters. For the algorithm-based parameters, the choices mainly affect the convergence speed and the stability of the algorithm used, so we carefully choose these values based on trial-and-error. For the model-based parameters, the segmentation results often depend on several main principal parameters, so we mainly tune these parameters in the numerical implementations. For the sake of simplification, we set these principal parameters in terms of a vector to represent the parameters in the modes (CV; GMAC; ICTM; WBHV; HLFRA; LBF; LIC; and OURS) in the order of $(\lambda; \gamma \text{ and } \lambda; \lambda \text{ and } \tau; \lambda \text{ and } r_3; \lambda_1, \lambda_2, \rho_1 \text{ and } \rho_2; \mu, \lambda_1 \text{ and } \tau; \mu \text{ and } \tau; \text{ and } \lambda)$, where ' $:$ ' is the separation mark. For the remaining parameters, we set $r = 1$ and $\tau = 0.001$ in [Algorithm 1](#); $r_1 = 1, r_2 = 2$ in the WBHV model; $\varphi_1 = \varphi_2 = 1, \epsilon = 1$ and $\sigma = 5$ in the HLFRA model; $v = 0.002 \times 255^2, \lambda_2 = 1$ and $\sigma = 3$ in the LBF model; and $v = 0.001 \times 255^2$ and $\sigma = 4$ in the LIC model.

4.2. Ultrasonic image segmentation

We first consider segmenting the region of interest (ROI) based on twelve ultrasound images from the breast dataset [47], as shown in [Fig. 1](#). For every segmentation model, we choose the same original contour.

The quantitative results are tabulated in the boxplots shown in [Fig. 2](#). It can be seen that JS, SA, F1-Score and κ generated by our proposed model are relatively shorter and higher than those generated by the other compared models. These facts imply the accurate and stable performance of our proposed model.

In addition, for visualization, we choose the segmentation results of ultrasound image #5, as shown in [Fig. 3](#). The results show that GMAC, HLFRA and LIC clearly do not segment the target object correctly, resulting in many unnecessary details. Although CV, ICTM, WBHV and LBF can roughly segment the object, their segmentation accuracy is not as good as the accuracy of our proposed method. It can also be seen from the mean value in [Table 1](#) that our model has the largest value compared to the other seven models, indicating that our segmentation results are closer to the ground truths.

To consider the effect of using different original contours on the segmentation results, we choose four initial contours for image #2 and then show the results in the first column in [Fig. 4](#). The corresponding segmentation results are shown in the second to ninth columns. It can be seen that the robustness of GMAC, WBHV, HLFRA, LBF, and LIC are more sensitive to the initial contour position than the robustness of CV, ICTM and our proposed model. After

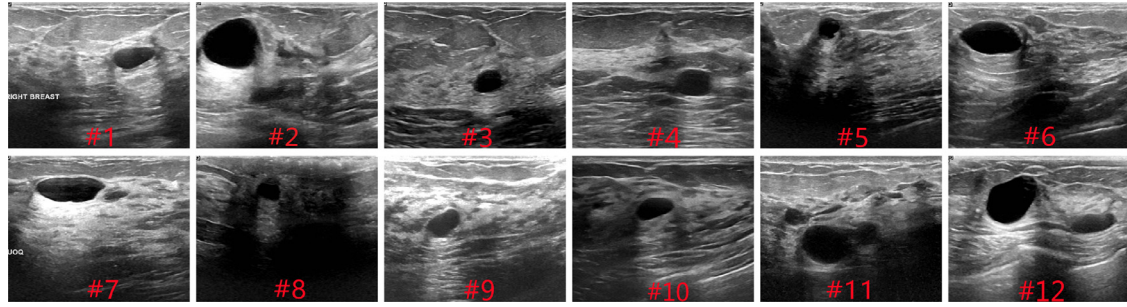


Fig. 1. Evaluation and comparison of ultrasound images from the breast ultrasound image dataset [47].

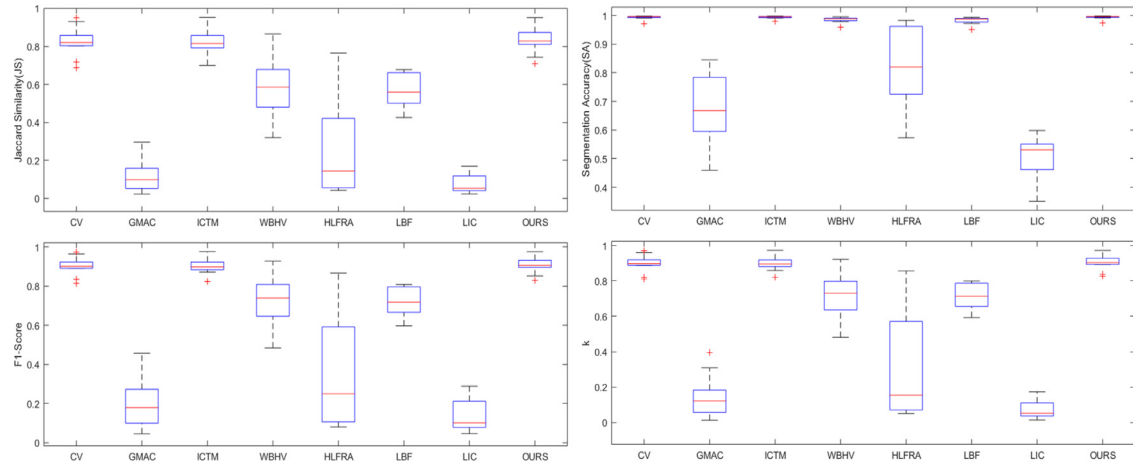


Fig. 2. Box plots of JS, SA, F1-Score and κ on twelve ultrasound images segmented by CV [26], GMAC [28], ICTM [38], WBHV [41], HLFRA [32], LBF [29], LIC [30] and OURS.

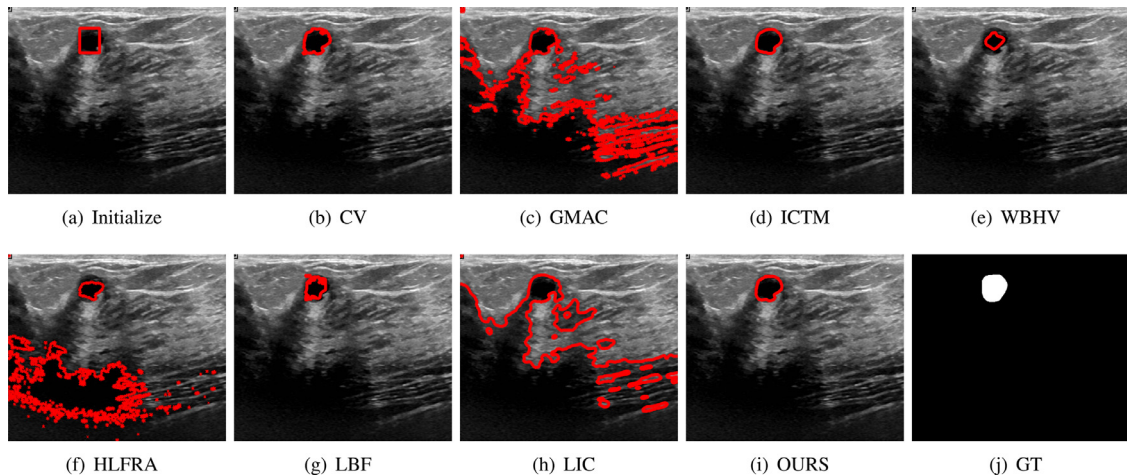


Fig. 3. Segmentation comparison on ultrasound image #5. From left to right: (a) the input 557×462 image with an initial contour; (b)-(i) segmentation results of CV [26], GMAC [28], ICTM [38], WBHV [41], HLFRA [32], LBF [29], LIC [30], and OURS; (j) ground truth. (The experimental parameters: (2; 0.0015 and 0.05; 0.005 and 0.001; 0.02 and 1; 65, 1, 0.1, and 0.1; 0.1, 1, and 0.1; 2 and 0.1; and 540)).

careful observation, CV causes edge leakage based on the choice of the position of the second initial contour, but ICTM and our proposed model can give more exact segmentation results. In addition, to further verify the robustness of two different initial contour positions, Fig. 5 shows the segmentation results obtained by the different models on image #2. It is obvious that these initial contours are quite different, but our proposed model can obtain almost the same results and capture the boundary correctly. This again proves the robustness of our proposed model to the initial contour choice.

In addition to the quantitative comparisons, we also compare the mean values of the CPU times of the eight models on twelve ultrasound images with a histogram. As seen from Fig. 6, the mean value of the CPU time of LBF is the largest, and our proposed model has the smallest mean CPU time among the WBHV, HLFRA and LBF models. This means that our proposed model achieves the best segmentation results in relatively little time.

The convergence of ADMM was established in [46] for a convex, closed and proper objective function, which is unfortunately

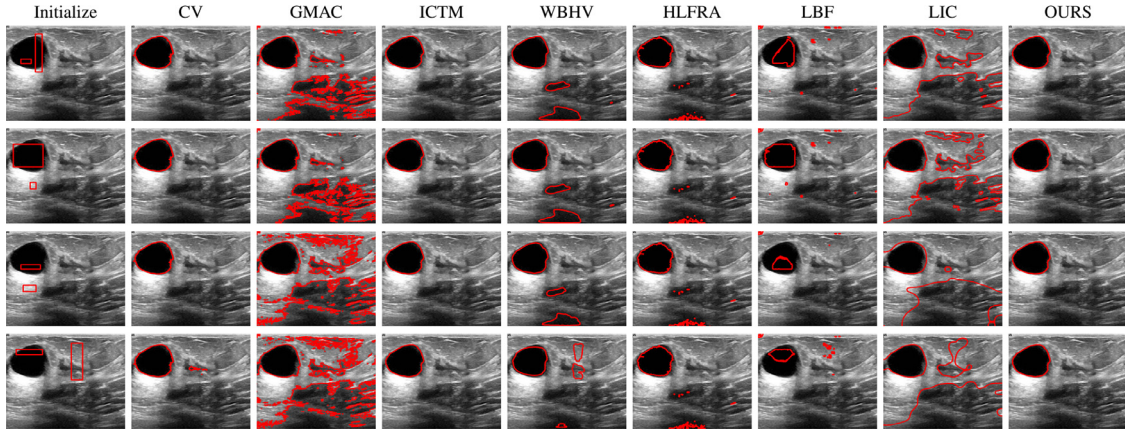


Fig. 5. Segmentation results of image #2 with four different initial contours (size:683 × 585). Column 1: different initializations. Columns 2 to 9: the corresponding segmentation results of the different segmentation methods.

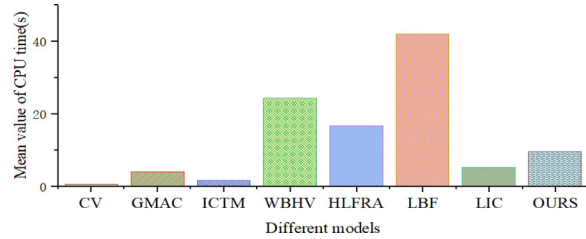


Fig. 6. Comparison of the mean values of the CPU times of the different models on twelve ultrasound images.

radiologists with over ten years of experience. And these images were also approved by the Medical Ethics Committee of Henan University of Chinese Medicine and the Medical Ethics Committee of United Imaging Healthcare. The original images and the corresponding ROIs are shown in Fig. 8 and Fig. 11.

Fig. 9 shows the experimental results of CV [26], GMAC [28], ICTM [38], WBHV [41], HLFRA[32], LBF[29], LIC[30] and our proposed model. Overall, the segmentation results of our proposed method are almost consistent with the expert segmentation re-

sults on 3T MR images. In addition, Fig. 9 clearly shows that the CV, GMAC, WBHV, HLFRA, LBF and LIC have worse segmentation results than ICTM and our proposed model. ICTM is obviously inferior to our proposed model on images #b and #f.

Fig. 11 shows that the segmentation results of our proposed model are similar to the ground truths on 5T MR images compared to the other seven models. Specifically, the CV, GMAC, WBHV, HLFRA, LIC models are easy to segment the non-target region in the process of segmenting the target region, such as the local enlarged region in the lower right corner of the first and third rows. The LBF model is difficult to segment the target region and the ICTM model does not accurately capture the boundary in some segmentation results. However, the segmentation results of our proposed model exhibit obvious superiority.

To ensure the accuracy of the analysis results, the quantitative indicators are also compared, as shown in Table 2 and Fig. 11. We find that the proposed method obtains the best segmentation result. For the Table 2, the boxplot in Fig. 10 more intuitively reflects that our method has short and higher JS, SA, F1-Score and κ values than the other seven models, which indicates that our proposed model is more accurate and stable.

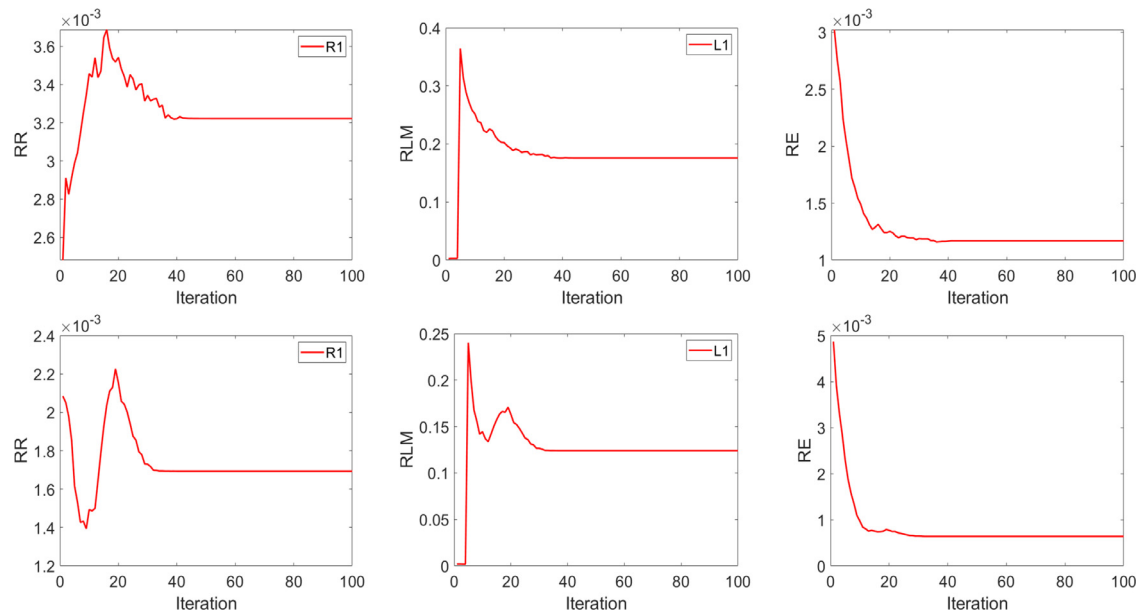


Fig. 7. Plots of the RR, RLM and RE against the number of iterations by using Algorithm 1 to segment images '#2' and '#12'.

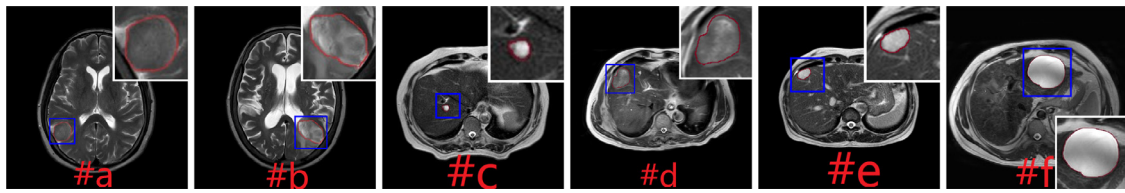


Fig. 8. Ground truths of six MR images #a to #f. The upper right corner or the lower right corner is the ROI.



Fig. 9. Segmentation comparison on 3T MR images. The first column shows the initial contours. The second column to the last column show the segmentation results of CV [26], GMAC [28], ICTM [38], WBHV [41], HLFRA [32], LBF [29], LIC [30] and OURS.

Table 2

The related results on six images of CV [26], GMAC [28], ICTM [38], WBHV [41], HLFRA [32], LBF [29], LIC [30] and OURS.

Criteria	JS								SA							
	CV	GMAC	ICTM	WBHV	HLFRA	LBF	LIC	OURS	CV	GMAC	ICTM	WBHV	HLFRA	LBF	LIC	OURS
Images	0.7444	0.0322	0.7105	0.0766	0.0597	0.6095	0.0223	0.7937	0.9975	0.7555	0.9975	0.9031	0.8838	0.9957	0.6441	0.9981
#a	0.8073	0.0595	0.6959	0.1100	0.2964	0.4151	0.0335	0.9186	0.9973	0.8116	0.9948	0.9209	0.9864	0.9904	0.6567	0.9990
#b	0.7953	0.0043	0.4103	0.0051	0.0041	0.3704	0.0019	0.7179	0.9998	0.8360	0.9995	0.8908	0.9022	0.9987	0.5744	0.9998
#c	0.7859	0.0362	0.8130	0.3557	0.0432	0.6389	0.0239	0.8267	0.9978	0.7887	0.9983	0.9947	0.8499	0.9967	0.6639	0.9985
#d	0.7705	0.0258	0.7365	0.3636	0.1466	0.5968	0.0104	0.7922	0.9991	0.8832	0.9990	0.9977	0.9902	0.9981	0.6506	0.9992
#e	0.7839	0.1577	0.7979	0.8040	0.1394	0.2049	0.2789	0.9558	0.9920	0.8436	0.9927	0.9940	0.8188	0.9712	0.9490	0.9987
Mean	0.7812	0.0526	0.6940	0.2858	0.1149	0.4726	0.0618	0.8342	0.9973	0.8198	0.9970	0.9502	0.9052	0.9918	0.6898	0.9989
Variance	0.0005	0.0030	0.0215	0.0866	0.0110	0.0295	0.0114	0.0078	0.0000	0.0020	0.0000	0.0026	0.0050	0.0001	0.0172	0.0000
Criteria	F1-Score								K							
Images	CV	GMAC	ICTM	WBHV	HLFRA	LBF	LIC	OURS	CV	GMAC	ICTM	WBHV	HLFRA	LBF	LIC	OURS
#a	0.8535	0.0623	0.8308	0.1423	0.1127	0.7574	0.0436	0.8850	0.8522	0.0473	0.8295	0.1292	0.0990	0.7552	0.0282	0.8840
#b	0.8934	0.1122	0.8207	0.1983	0.4573	0.5867	0.0649	0.9575	0.8920	0.0918	0.8181	0.1811	0.4504	0.5818	0.0428	0.9570
#c	0.8860	0.0085	0.5818	0.0101	0.0081	0.5405	0.0037	0.8358	0.8859	0.0070	0.5816	0.0085	0.0066	0.5400	0.0021	0.8357
#d	0.8801	0.0699	0.8969	0.5247	0.0827	0.7797	0.0467	0.9051	0.8790	0.0549	0.8960	0.5227	0.0682	0.7780	0.0311	0.9043
#e	0.8704	0.0504	0.8483	0.5333	0.2556	0.7475	0.0205	0.8841	0.8699	0.0436	0.8478	0.5324	0.2517	0.7466	0.0134	0.8837
#f	0.8789	0.2725	0.8876	0.8914	0.2447	0.3401	0.4362	0.9774	0.8747	0.2334	0.8839	0.8883	0.2034	0.3272	0.4128	0.9767
Mean	0.8771	0.0960	0.8110	0.3834	0.1935	0.6253	0.1026	0.9075	0.8756	0.0797	0.8095	0.3770	0.1799	0.6215	0.0884	0.9069
Variance	0.0002	0.0086	0.0135	0.1065	0.0259	0.0293	0.0272	0.0027	0.0002	0.0064	0.0134	0.1085	0.0256	0.0306	0.0255	0.0027

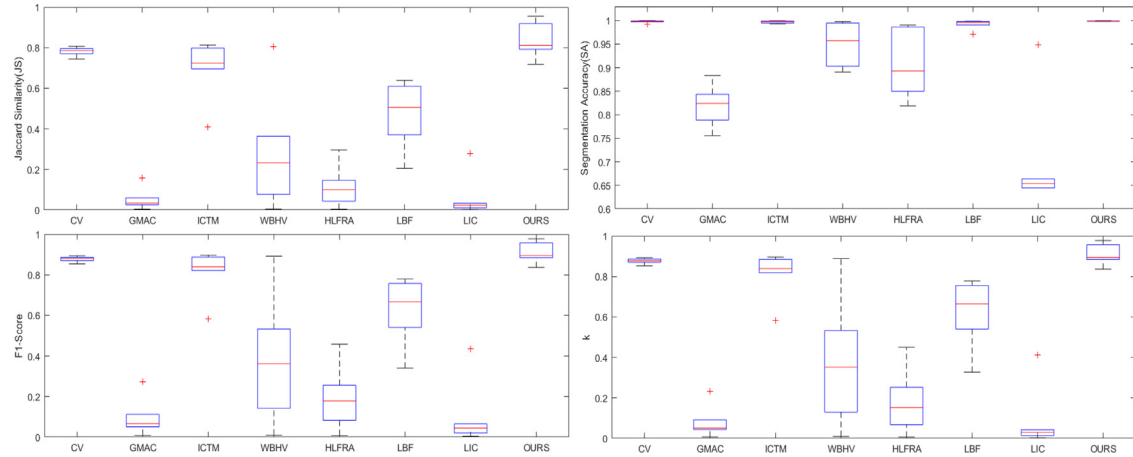


Fig. 10. The related results on six 3T MR images of CV [26], GMAC [28], ICTM [38], WBHV [41], HLFRA [32], LBF [29], LIC [30] and OURS.

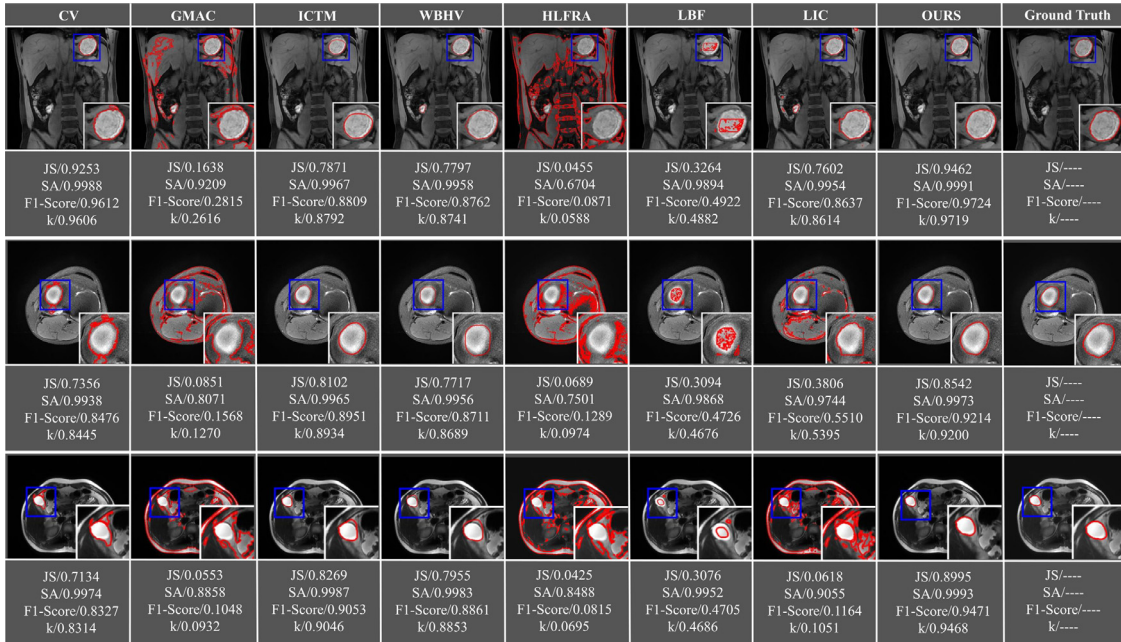


Fig. 11. Comparison of the segmentation methods on three 5T MR images. The first column to the eighth column show the segmentation results of CV [26], GMAC [28], ICTM [38], WBHV [41], HLFRA [32], LBF [29], LIC [30] and OURS.

4.4. Multiphase brain MR image segmentation

For the multiphase case, we set $n = 4$. Since several models are only suitable for segmenting two-phase images, we only choose three models, CV, ICTM and WBHV, to compare with our proposed model for segmenting brain MR images³. These brain images are divided into four parts: cerebrospinal fluid (CF), gray matter (GM), white matter (WM) and background. We randomly selected ten brain MR images as test images. In Fig. 12, the average JS, SA, F1-Score and κ values for CF, GM and WM obtained by the models are shown through histograms, which demonstrate that our proposed method achieves better performance when segmenting these images.

To intuitively compare these segmentation results, we randomly select three images from ten test images to display the results. Three brain MR images #A, #B and #C with a size of 181×217

are exhibited in the first row of Fig. 13. We set the maximum number of iterations to $K_{\max} = 50$ and the stopping thresholds to $RE \leq 10^{-3}$, $r = 2$, and $\tau = 0.01$ for our proposed model. The parameter is chosen as $\lambda = \{10, 15, 8\}$ for three images #A, #B and #C. The experimental results of CV, ICTM, WBHV and our proposed model are exhibited from the second row to the fifth row. The ground truths are displayed in the last row. The first three columns are CF, GM and WM for image #A. The middle three columns are CF, GM and WM for image #B, and the last three columns are CF, GM and WM for image #C. Fig. 13 shows that our proposed method can detect more CF than CV and capture more GM than ICTM and WBHV. In other words, under segmentation of GM occurs in the CV model. Since these four methods have very similar segmentation results to the ground truth, it is difficult to rate the quality of different segmentation results via global visual judgement. Therefore, the red box and blue box areas in Fig. 14 are enlarged to compare the segmentation details. The results show that our proposed model can obtain more accurate segmentation results.

³ <https://brainweb.bic.mni.mcgill.ca/>.

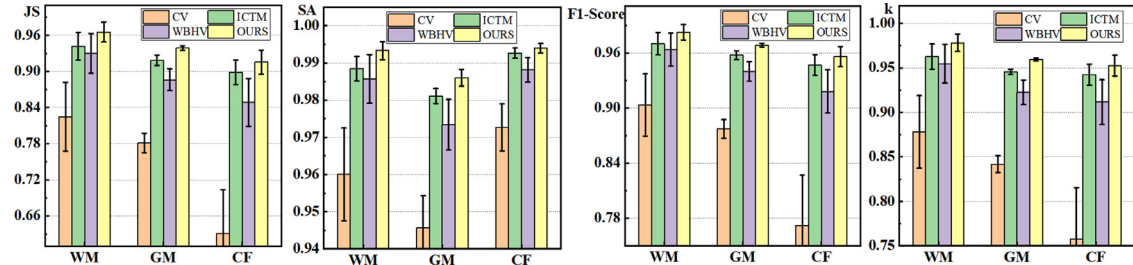


Fig. 12. Statistical results (JS, SA, F1-Score, κ) on ten brain MR images for WM, GM, and CF tissues.

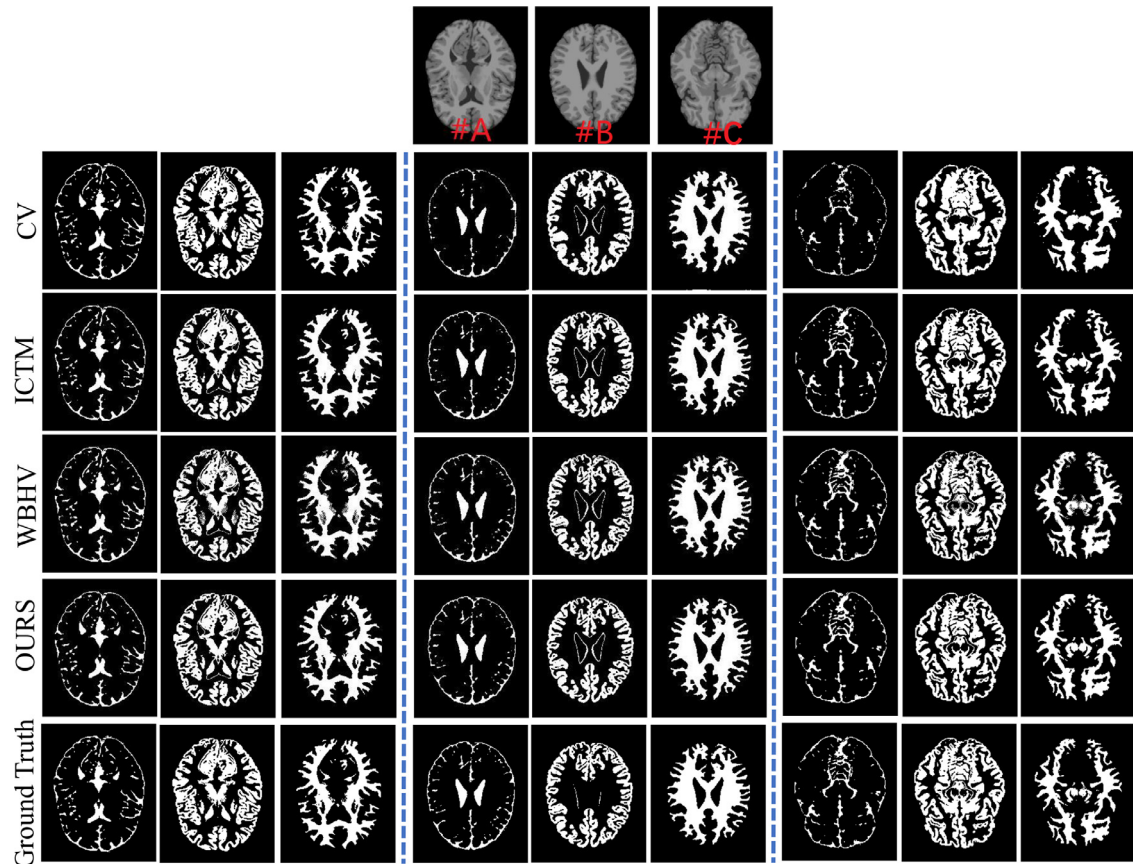


Fig. 13. Comparison of the segmentation methods on three brain MR images. The first row: images #A, #B and #C. The second row to the fifth row: the segmentation results of CV, ICTM, WBHV and OURS for all three tissues, i.e., CF, GM and WM. The last row: the ground truth.

5. Discussion and conclusion

In this study, we focus on traditional model-driven models to segment medical images. For the proposed model, the heat kernel convolution operation is utilized to approximate the perimeter of the segmentation curve, which can reduce the computational complexity of the WBHV model by reducing the number of manually adjusted parameters. Furthermore, the weight in the high-order total variation term can be automatically adjusted according to the input image to enhance the features of the local structure and improve the segmentation accuracy. However, Data-driven models not only need a large amount of data for training but also need manual labeling by experts, which causes a high computational burden and manpower waste. In addition, data-driven models do not have strict mathematical theoretical knowledge to explain the meaning of the model and are not robust to adversarial samples. On the contrary, the advantages of traditional model-driven models are

that they do not rely on a large number of manual markers and have good interpretability in mathematical theory. For this purpose, this paper mainly considers model-driven models.

For our proposed segmentation model, our work is not only applicable to medical image segmentation, but also to natural image segmentation. But in this experiment, we mainly focus on medical images. In addition, a limitation of our proposed approach is that the parameter λ in the model needs to be tried manually, which leads to a lot of inconvenience.

In the future, we would like to study how to incorporate the proposed model into a deep learning network so that the hyperparameter λ can be learned during the training process. At the same time, we would study the network iteration model and apply the proposed model to different scene segmentation tasks. Additionally, we will continue to improve our model and algorithm in mathematical theory to obtain higher segmentation accuracy. Furthermore, we will also use our model and algorithm to improve

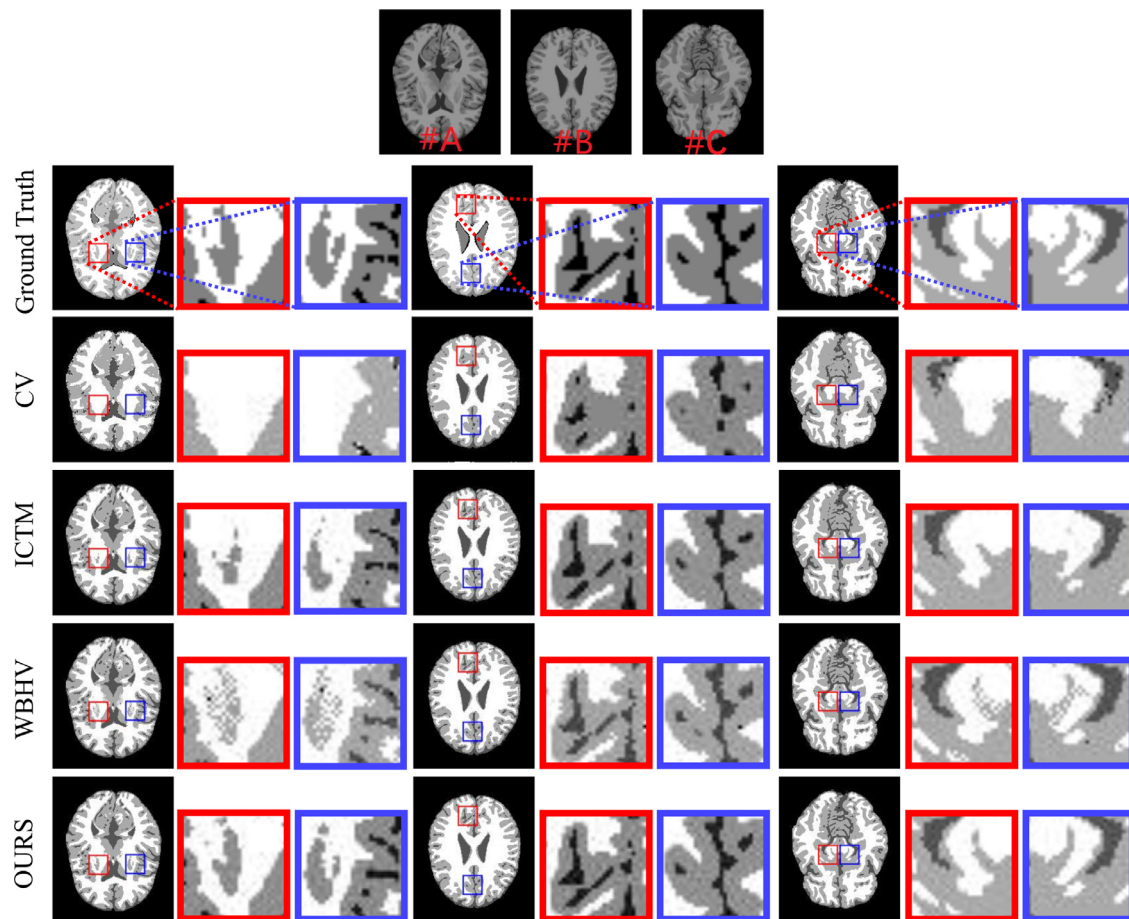


Fig. 14. Comparison of two brain MR image segmentations. The first row: images #A, #B and #C. The second row: the ground truth. The third row to the sixth row: the segmentation results of CV, ICTM, WBHV and OURS. The second column, the fifth column and the eighth column are partial enlargements of the red boxes. The third column, the sixth column and the ninth column are partial enlargements of the blue boxes. (For interpretation of the references to colour in this figure legend, the reader is referred to the web version of this article.)

the efficiency of the algorithm in practical applications through GPU acceleration. Moreover, we would explore a more accurate and interpretable medical image segmentation model, which is an important future direction.

In conclusion, this work represents a novel adaptive weighted curvature-based active contour for medical image segmentation. To describe local structures and establish an efficient numerical algorithm, we employed weights to adaptively penalize the high-order total variation and used the heat kernel convolution operation to approximate the total variation to improve the numerical method. Since the improved model is nonsmooth, ADMM can be used to solve the proposed model. The experimental results on ultrasonic and 3T/5T MR images are compared with those of other algorithms to show the robustness of our proposed method.

Declaration of Competing Interest

The authors declare that they have no known competing financial interests or personal relationships that could have appeared to influence the work reported in this paper.

CRediT authorship contribution statement

Zhi-Feng Pang: Conceptualization, Formal analysis, Validation, Writing – original draft, Writing – review & editing. **Mengxiao Geng:** Conceptualization, Formal analysis, Validation, Writing – original draft, Writing – review & editing. **Lan Zhang:** Conceptualization, Formal analysis, Validation, Writing – original draft,

Writing – review & editing. **Yanru Zhou:** Conceptualization, Formal analysis, Validation, Writing – original draft, Writing – review & editing. **Tieyong Zeng:** Conceptualization, Formal analysis, Validation, Writing – original draft, Writing – review & editing. **Liyun Zheng:** Conceptualization, Formal analysis, Validation, Writing – original draft, Writing – review & editing. **Na Zhang:** Conceptualization, Formal analysis, Validation, Writing – original draft, Writing – review & editing. **Dong Liang:** Conceptualization, Formal analysis, Validation, Writing – original draft, Writing – review & editing. **Hairong Zheng:** Conceptualization, Formal analysis, Validation, Writing – original draft, Writing – review & editing. **Yongming Dai:** Conceptualization, Formal analysis, Validation, Writing – original draft, Writing – review & editing. **Zhenxing Huang:** Conceptualization, Formal analysis, Validation, Writing – original draft, Writing – review & editing. **Zhanli Hu:** Conceptualization, Formal analysis, Validation, Writing – original draft, Writing – review & editing.

Data availability

Data will be made available on request.

Acknowledgments

This work was supported by the National Natural Science Foundation of China (grants: 12071345, 32022042, 81871441, 62101540), the Programs for Science and Technology Development of Henan Province (grants: 212102210511,

212102310732), the SKY research programme (grant: Z-2014-07-2101), the Science and Technology Major Project of Henan Province (grant: 221100310200), the Shenzhen Excellent Technological Innovation Talent Training Project of China (grant: RCJC20200714114436080), the Shenzhen Science and Technology Program (grant: RCBS20210706092218043), the [China Postdoctoral Science Foundation](#) (grant: 2022M713290), and the Guangdong Innovation Platform of Translational Research for Cerebrovascular Diseases of China.

References

- [1] H. Yu, S. Wang, W. Wu, C. Gong, L. Wang, Z. Pi, F. Liu, Weighted adaptive non-local dictionary for low-dose CT reconstruction, *Signal Processing* 180 (2021).
- [2] H. Wang, Z. Huang, Q. Zhang, D. Gao, Z. Ou Yang, D. Liang, X. Liu, Y. Yang, H. Zheng, Z. Hu, A preliminary study of dual-tracer PET image reconstruction guided by FDG and/or MR kernels, *Med Phys* 48 (9) (2021) 5259–5271.
- [3] P. Zhuang, X. Zhu, X. Ding, MRI reconstruction with an edge-preserving filtering prior, *Signal Processing* 155 (2019) 346–357.
- [4] A. Ghanbarzadeh-Dagheyan, J. Heredia-Juesas, C. Liu, A. Molaei, J.A. Martinez-Lorenzo, B.V. Vahdat, M.T. Ahmadian, A holey cavity for single-transducer 3d ultrasound imaging with physical optimization, *Signal Processing* 179 (2021) 107826.
- [5] S. Duncan, N. Ayache, Medical image analysis: progress over two decades and the challenges ahead, *IEEE Trans Pattern Anal Mach Intell* 22 (1) (2000) 181–204.
- [6] D. Shen, G. Wu, H. Suk, Deep learning in medical image analysis, *Annu Rev Biomed Eng* 19 (2017) 221–248.
- [7] X. Zhang, G. Weng, Level set evolution driven by optimized area energy term for image segmentation, *Optik (Stuttgart)* 168 (2018) 517–532.
- [8] M. Gou, Y. Rao, M. Zhang, J. Sun, K. Cheng, Automatic image annotation and deep learning for tooth CT image segmentation, *International Conference on Image and Graphics* (2019) 519–528.
- [9] M. Khan, M. Gajendran, Y. Lee, M. Khan, Deep neural architectures for medical image semantic segmentation: review, *IEEE Access* 9 (2021) 83002–83024.
- [10] S. Minaee, Y. Boykov, F. Porikli, A. Plaza, N. Kehtarnavaz, D. Terzopoulos, Image segmentation using deep learning: a survey, *IEEE Trans Pattern Anal Mach Intell* (2021).
- [11] F. Sultana, A. Sufian, P. Dutta, Evolution of image segmentation using deep convolutional neural network: a survey, *Knowl Based Syst* 201 (2020) 106062.
- [12] M. Falcone, G. Paolucci, S. Tozza, A high-order scheme for image segmentation via a modified level-set method, *SIAM J Imaging Sci* 13 (1) (2020) 497–534.
- [13] M. Unger, T. Pock, W. Trobin, D. Cremers, H. Bischof, TVSeg-Interactive Total variation based image segmentation, *Proceedings of the British Machine Vision Conference* (2008).
- [14] V. Djordjevic, V. Stojanovic, H. Tao, X. Song, S. He, W. Gao, Data-driven control of hydraulic servo actuator based on adaptive dynamic programming, *Discrete and Continuous Dynamical Systems-S* 15 (7) (2022) 1633.
- [15] M. Daoud, A. Atallah, F. Awwad, M. Al-Najjar, R. Alazrai, Automatic superpixel-based segmentation method for breast ultrasound images, *Expert Syst Appl* 121 (2019) 78–96.
- [16] Q. Ma, T. Zeng, D. Kong, J. Zhang, Weighted area constraints-based breast lesion segmentation in ultrasound image analysis, *Inverse Problems and Imaging* (2021), doi:[10.3934/ipi.2021057](https://doi.org/10.3934/ipi.2021057).
- [17] B. Li, J. Qin, R. Wang, M. Wang, X. Li, Selective level set segmentation using fuzzy region competition, *IEEE Access* 4 (2016) 4777–4788.
- [18] L. Vese, T. Chan, A multiphase level set framework for image segmentation using the mumford and shah model, *Int J Comput Vis* 50 (2002) 271–293.
- [19] Y. Zhou, W. Shi, W. Chen, Y. Chen, Y. Li, L. Tan, D. Chen, Active contours driven by localizing region and edge-based intensity fitting energy with application to segmentation of the left ventricle in cardiac CT images, *Neurocomputing* 156 (2015) 199–210.
- [20] A. Rahmandinof, F. Nazir, Y. Dwihapsari, Image segmentation of thyroid SPECT using edge-based active contour model, *J. Phys. Conf. Ser.* (2020).
- [21] G. Sapiro, Vicent caselles, ron, and geodesic active contours, *Int J Comput Vis* 22 (1997) 61–79.
- [22] J. Fang, H. Liu, J. Liu, H. Zhou, L. Zhang, H. Liu, Fuzzy region-based active contour driven by global and local fitting energy for image segmentation, *Appl Soft Comput* (2021).
- [23] K. Zhang, H. Song, L. Zhang, Active contours driven by local image fitting energy, *Pattern Recognit* 43 (4) (2010) 1199–1206.
- [24] M. Srikanth, Active contours segmentation with edge based and local region based, *Proceedings of the 21st International Conference on Pattern Recognition* (2012).
- [25] A. Niaz, K. Rana, A. Joshi, A. Munir, D. Kim, H. Song, K. Choi, Hybrid active contour based on local and global statistics parameterized by weight coefficients for inhomogeneous image segmentation, *IEEE Access* 8 (2020) 57348–57362.
- [26] T. Chan, L. Vese, Active contours without edges, *IEEE Trans. Image Process.* 10 (2) (2001) 266–277.
- [27] T. Chan, S. Esedoglu, M. Nikolova, Algorithms for finding global minimizers of image segmentation and denoising models, *SIAM J Appl Math* 66 (5) (2006) 1632–1648.
- [28] X. Bresson, S. Esedoglu, P. Vandergheynst, J. Thiran, S. Osher, Fast global minimization of the active contour/snake model, *J Math Imaging Vis* 28 (2007) 151–167.
- [29] C. Li, C. Kao, J. Gore, Z. Ding, Minimization of region-scalable fitting energy for image segmentation, *IEEE Trans. Image Process.* 17 (2008) 1940–1949.
- [30] C. Li, R. Huang, Z. Ding, C. Gatenby, D. Metaxas, J. Gore, A level set method for image segmentation in the presence of intensity inhomogeneities with application to MR, I, *IEEE Transactions on Image Processing* 20 (7) (2011) 2007–2016.
- [31] S. Krinidis, V. Chatzis, Fuzzy energy-based active contour, *IEEE Trans. Image Process.* 18 (12) (2009) 2747–2755.
- [32] J. Fang, H. Liu, L. Zhang, H. Liu, Region-edge-based active contours driven by hybrid and local fuzzy region-based energy for image segmentation, *Inf Sci (Ny)* 546 (2021) 397–419.
- [33] A. Beck, *First-order Methods in Optimization*, SIAM, 2017.
- [34] M. Benning, M. Burger, Modern regularization methods for inverse problems, *Acta Numerica* 27 (2018) 1–111.
- [35] V. Stojanovic, N. Nedic, Joint state and parameter robust estimation of stochastic nonlinear systems, *Int. J. Robust Nonlinear Control* 26 (14) (2016) 3058–3074.
- [36] Z. Xu, X. Li, V. Stojanovic, Exponential stability of nonlinear state-dependent delayed impulsive systems with applications, *Nonlinear Anal. Hybrid Syst* 42 (2021).
- [37] X. Zhang, H. Wang, V. Stojanovic, P. Cheng, S. He, X. Luan, F. Liu, Asynchronous fault detection for interval type-2 fuzzy nonhomogeneous higher-level Markov jump systems with uncertain transition probabilities, *IEEE Trans. Fuzzy Syst.* (2021).
- [38] D. Wang, X. Wang, The iterative convolution-thresholding method (ICTM) for image segmentation, *Pattern Recognit* (2022).
- [39] S. Esedoglu, F. Otto, Threshold dynamics for networks with arbitrary surface tensions, *Commun Pure Appl Math* 68 (5) (2014) 808–864.
- [40] M. Miranda, D. Pallara, F. Paronetto, M. Preunkert, Short-time heat flow and functions of bounded variation in \mathbb{R}^n , *Annales dela faculte des sciences de Toulouse Mathematiques* 16 (1) (2007) 125–145.
- [41] Y. Yang, Q. Zhong, Y. Duan, T. Zeng, A weighted bounded hessian variational model for image labeling and segmentation, *Signal Processing* (2020).
- [42] D. Mumford, J. Shah, Optimal approximations by piecewise smooth functions and associated variational problems, *Commun Pure Appl Math* 42 (1989) 577–685.
- [43] M. Fukushima, Application of the alternating direction method of multipliers to separable convex programming problems, *Comput Optim Appl* 1 (1992) 93–111.
- [44] C. Liu, W. Liu, W. Xing, An improved edge-based level set method combining local regional fitting information for noisy image segmentation, *Signal Processing* 130 (2017) 12–21.
- [45] A. Nia, A. Memon, K. Rana, A. Joshi, S. Soomro, J. Kang, K. Choi, Inhomogeneous image segmentation using hybrid active contours model with application to breast tumor detection, *IEEE Access* 8 (2020) 186851–186861.
- [46] R. Glowinski, S. Osher, W. Yin, *Splitting Methods in Communication, Imaging, Science, and Engineering*, Springer, 2016.
- [47] W. Al-Dhabyani, M. Gomaa, H. Khaled, A. Fahmy, Dataset of breast ultrasound images, *Data Brief* 28 (2020) 104863.